Cement & Concrete Composites 45 (2014) 57–68

Contents lists available at ScienceDirect

Cement & Concrete Composites

journal homepage: www.elsevier.com/locate/cemconcomp

Methodology for nanoindentation-assisted prediction of macroscale elastic properties of high performance cementitious composites

W.R.L. da Silva [a,*], J. Němeček [a], P. Štemberk [b]

[a] Faculty of Civil Engineering, Department of Mechanics, Thákurova 7, 166 29 Prague 6, Czech Republic
[b] Faculty of Civil Engineering, Department of Concrete and Masonry Structures, Thákurova 7, 166 29 Prague 6, Czech Republic

ARTICLE INFO

Article history:
Received 21 October 2011
Received in revised form 8 August 2013
Accepted 16 September 2013
Available online 25 September 2013

Keywords:
Nanoindentation
Multiscale analysis
Homogenization
Elastic modulus
High performance cementitious composite

ABSTRACT

This paper describes a methodology applied for determination of macroscale elastic properties of high performance cementitious composites (HPCC) based on nanoindentation measurements. For that, the elastic properties of HPCC mixtures with quartz filler and fly ash were evaluated at different length scales by nanoindentation (microscale) and the static and dynamic elastic moduli and compressive strength tests (macroscale). The nanoindentation results, obtained from a representative microlevel area by grid indentation with subsequent phase deconvolution, were complemented by an independent porosimetry test and inserted into a two-step analytical homogenization scheme to predict the overall macroscale properties. The final results indicate that the presented methodology allows a reliable advanced prediction of HPCC elastic properties, which is promising for the concrete industry since it would allow for reducing the number of large scale experiments and producing of a more predictable composite in an easier and experimentally less expensive way.

1. Introduction

Nowadays, cementitious composites, which include various types of concretes and mortars, represent the most used building materials. To a certain extent, and often with a trace of hope, concrete and mortar mixtures can be considered as homogeneous materials. However, this classification may change according to the level of observation (micro, meso, and macroscopic level). Those materials whose homogeneity depends on the observation level are called multiscale materials. With the scope of this definition, cementitious composites are the typical representatives of multiscale materials since they can be treated as homogeneous in the macroscopic level (cm–m length scale) and as heterogeneous material in a finer level of observation (nm–cm length scale).

Heterogeneity at the lower level comes from both the chemical reactions (e.g. hydration process [1,2]) and the mechanical mixing of non-reactive components (e.g. aggregate particles [3,4]). Further, transition zones between the phases and also porosity are present at each scale of the composite. The multiscale analysis of a composite involves the following steps: (i) microstructure observation (i.e. determination of morphological parameters) and separation of chemically different phases, (ii) assessment of mechanical properties of individual phases and their links to chemical properties, and (iii) upscaling of properties from the microlevel to a broader scale [3,5]. The microstructure observation and determination of phases can be performed, e.g. by analysis of images obtained from optical microscopy, scanning electron microscopy (SEM), or atomic force microscopy (AFM). Several researches [4–8] have been using successfully these techniques to obtain morphological and chemical parameters of individual material phases, and equally as in this paper, the microstructure analysis has often been supplemented by porosity measurements (e.g. mercury intrusion porosimetry) and/or image analysis.

The micromechanical analysis of individual material phases (nm–μm scale) can be obtained exclusively by the nanoindentation technique, which is used for assessing the mechanical properties of small volumes at nano and microlevel. The principle of nanoindentation lies in forcing a very small tip (typically diamond) to the material surface while the changes in the applied load and the penetration depth are measured simultaneously [9]. By using this technique, material properties, such as elastic modulus, hardness and plastic or viscous parameters, can be obtained from experimental readings for a given material volume [9–11]. The macrolevel analysis is performed by different types of standardized macroscopic tests (e.g. by the static compression, tension or bending, and/or by dynamic tests) in which the overall material properties are obtained on large specimens (cm–m scale).

The transition between micro and macrolevels can be treated with a micromechanical approach that separates the levels by defining a characteristic scale and related representative volume

* Corresponding author.
E-mail addresses: wilson.silva@fsv.cvut.cz (W.R.L. da Silva), jiri.nemecek@fsv.cvut.cz (J. Němeček), stemberk@fsv.cvut.cz (P. Štemberk).

0958-9465/$ - see front matter © 2013 Elsevier Ltd. All rights reserved.
http://dx.doi.org/10.1016/j.cemconcomp.2013.09.013

elements (RVE) for each of the levels [12]. The response of the micromechanically heterogeneous RVE can be averaged through different homogenization techniques that aim at replacing the microscopically inhomogeneous strains and stresses by their fictitious homogeneous (effective) counterparts [12–14]. A significant group of analytical methods is based on the classical Eshelby's solution of ellipsoidal inclusions embedded in a matrix [13], namely the Mori–Tanaka method, the self-consistent scheme, and others [12]. Numerical homogenizations can include finite element computations or fast-Fourier transformation [14–16]. Among the analytical homogenization schemes, the Mori–Tanaka method is used frequently for its simplicity and wide applicability in terms of the concentration range of the multiple phases that are involved. Its performance was also justified by some researchers when used for cementitious composites [3,5,17].

In this paper, a proposed methodology that is based on the combination of the above mentioned techniques and approaches has been applied in order to determine macroscale elastic properties of the high performance cementitious composites (HPCC) [18] based on nanoindentation measurements. By defining the link between microstructure, micromechanical properties, and macroscopic mechanical performance of such a cementitious material, one can optimize the mechanical properties of the composite in an easier and experimental less expensive way. When combining the aforementioned advantages, the proposed methodology for nanoindentation-assisted prediction of mechanical properties of cementitious composites can be highly inviting for the concrete industry, since they would be able to deliver a more predictable product, i.e. the high performance concrete with the desired elastic properties that were selected as the most important mechanical parameters for the initial mixture optimization.

2. Proposed methodology for prediction of macroscale elastic properties of HPCC

The demand for high performance properties, such as high compressive strength or Young's modulus, has been increasing due to the needs of the new construction developments, e.g. skyscrapers, bridges with challenging architectural designing, precast concrete structures, etc. Nowadays, the production and application of HPCC is already a reality in the concrete industry. However, the application of this composite is always surrounded by a vast number of experimental tests, which leads to a considerable production cost, to ensure that its properties will be achieved. Aiming to reduce the experimental work, and thus production costs, necessary to design HPCC and to allow the concrete industry for delivering a more predictable product, a different approach has to be considered in the design/testing methodology. This approach could, for instance, consider the use of microscale analysis in order to predict the macroscale properties of the composite. Bearing in mind this idea, the following methodology is proposed.

The methodology conceives the solution to this problem in the same way as it is dealt by the industry, which is, first of all, defining the ultimate properties of the desired product, in this case, the hardened (compressive strength and elastic modulus) and fresh state properties (workability and entrained air) of the concrete. After that, the properties, especially the fineness, grain size distribution, and aggregates elastic modulus, of the materials that will be used to produce the HPCC mixtures are defined.

Subsequently, the initial composition is defined based on either previous experimental experiences or designing methods. Next, the mixtures are prepared and its fresh state properties are verified. Notice that the experiments necessary to test the properties on the fresh state varies according to the type of mixture to be produced (e.g. self-compacting concrete would require slump-flow tests, while mortar mixtures would require flow-table test).

Once the fresh state properties have been achieved, the specimens for microscale and macroscale tests are casted and then cured for a defined period. The macroscale tests on the hardened state include the determination of the compressive strength, static and dynamic elastic modulus, while the microscale tests include porosity analysis at various observation levels, which are defined by the designers according to the RVE size, and grid nanoindentation tests. The nanoindentation tests parameters, such as grid indentation size and depth of penetration, are defined based also on the RVE size, which is set by the designers depending on the actual microstructural situation. Notice that, in this paper, the RVE size of the lower level has been set at $\approx$100 μm to include all the matrix phases. In total, the microstructure of the analyzed composite was split in two levels: matrix and mortar, named as Level I and II respectively.

The results from the nanoindentation tests on the Level I are then evaluated by statistical deconvolution in order to define the properties of the individual phases in the assessed composite and by analytical homogenization. Once the microstructure levels have been defined, the upscaling of properties from the microlevel to a higher scale is performed by means of the Mori–Tanaka homogenization scheme [19], which is applied at each different level and computes the homogenized elastic modulus (E_{hom}) and Poisson's ratio (ν_{hom}). The Level I homogenized results are verified by using a fast-Fourier transformation based scheme [14], while the results from Level II, which corresponds to the whole composite itself, are verified by the results from the experimental macroscale elastic tests. This final verification permits to define the prediction uncertainty and validate the proposed methodology.

The flowchart of the abovementioned prediction methodology and the experimental analyses applied to verify and validate the predicted results are illustrated in Fig. 1. The detailed description of the concepts and experimental tests included in this methodology are discussed in this paper. It is important to bear in mind that the proposed methodology consists in an iterative process. However, as this work aims to determine macroscale elastic properties of the HPCC based on nanoindentation measurements, only one part of the iteration process will be tested (see detail in Fig. 1). The full iteration process shall be tested in the upcoming research.

3. Experimental program and evaluation of results

In this section, the details on the tested materials, mixture compositions, sample preparation, mixing procedure, and tests performed are given. Also, the experimental setup for the analysis of mechanical properties at micro and macroscopic levels are presented.

3.1. Materials

The tests conducted in this study were carried out with previously optimized mortar mixtures, further denoted as C1 and C2, produced with different materials. Both mortar mixtures contained cement CEM II/A-S 52.5 N, whose chemical composition is indicated in Table 1, and the high-range water reducing admixture (HRWRA) Stachement 2000. The mixture C1 contained quartz filler (provided by Sklopísek Střeleč, CZ) with the maximum grain size of 0.063 mm, whereas fly ash (from the brown coal power plant Ledvice, CZ) was used for preparation of C2.

A mix of two fine quartz sands (ST06/12 and ST01/06, provided by Sklopísek Střeleč, CZ) with different grain size limits were used as aggregates. The sand mix included 50 vol.% of ST06/12 (with the grain size range varying from 0.63 mm to 1.25 mm) and 50 vol.% of

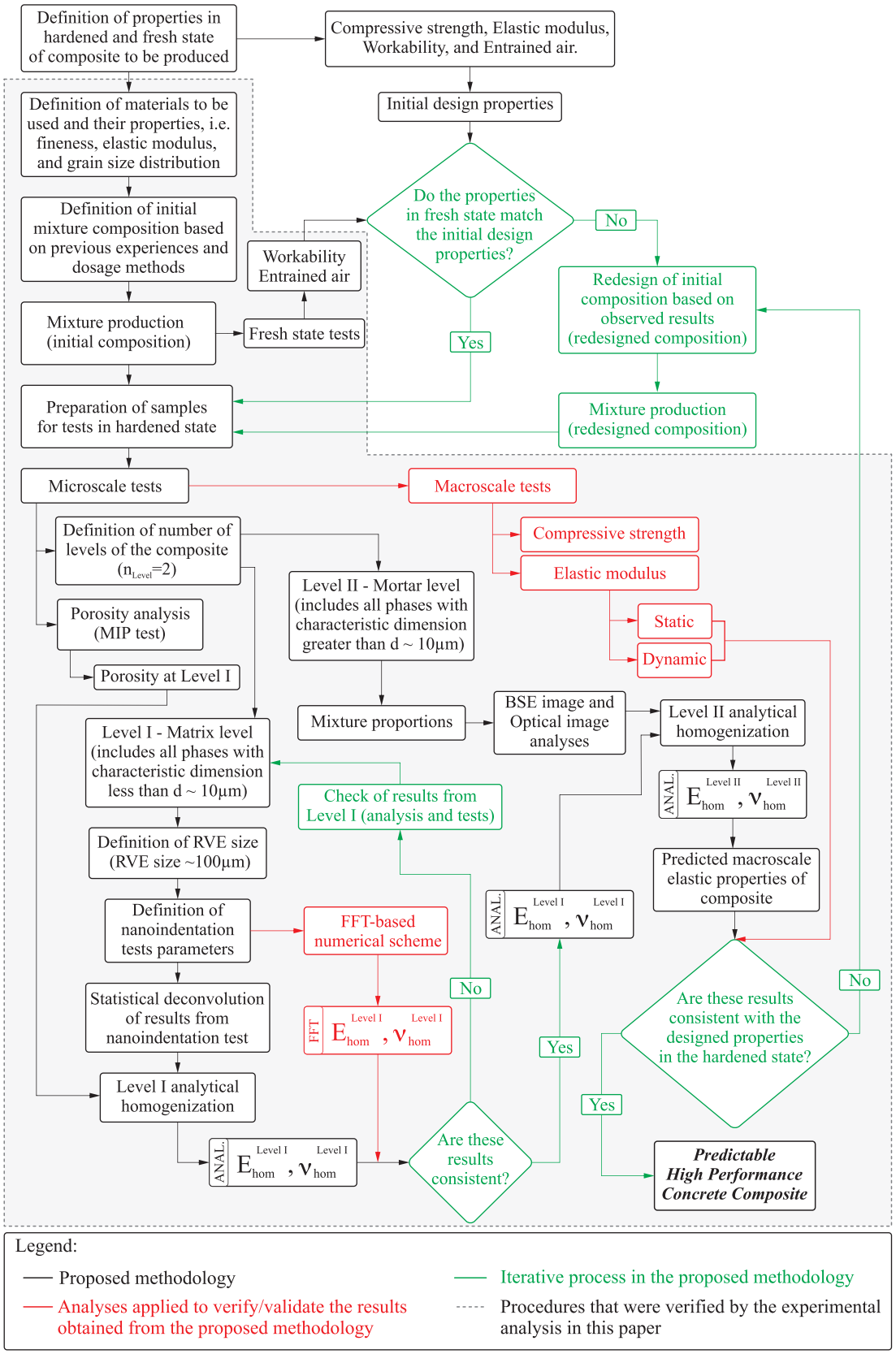

Fig. 1. Flowchart of the methodology for prediction of macroscale elastic properties of HPCC.

ST01/06 (with the grain size range varying from 0.10 mm to 0.63 mm). The grain size distribution of both the aggregates is listed in Table 2. The aggregates are mainly composed of SiO_2 (99.2%) and Fe_2O_3 (0.04%). The chemical composition of a typical brown coal fly ash sample (class F, Blaine specific surface ≈210 $m_{2/kg}$) is shown in Table 3.

Table 1
Chemical composition of CEM II/A-S 52.5 N (wt.%).

	%
CaO	57.6
SiO_2	21.1
Al_2O_3	6.2
Fe_2O_3	3.6
MgO	1.7
Na_2O	0.40
K_2O	0.69
SO_3	3.3
Cl^-	0.06
Loss on ignition	1.5
Insolubles	0.3

Table 2
Grain size distribution of aggregates (in wt.%).

	ST 01/06	ST 06/12
Middle grain size, d^{50} (mm)	0.38	0.88
AFS grain fineness number	30	14
Bulk density (kg/m^3)	1500	1600
Grain size (μm)		
>4000	–	–
>1250	–	7.0%
>1000	0.0%	–
>800	–	–
>630	12.0%	91.0%
>315	–	–
>200	85.0%	–
>100	2.0%	–
<100	1.0%	2.0%

3.2. Mixture compositions, mixing procedure and fresh state tests

The compositions of the mortar mixtures in mass and volume are presented in Table 4. These compositions were defined based on previous study results [20] and adjusted, with a lower w/c ratio, in order to obtain higher compressive strength. Due to the different density of the fly ash and quartz filler, it was necessary to apply volumetric substitution of the additives in order to keep the cement content constant in C1 and C2. The mixing procedure described in Table 5 was applied for both the mixtures. Once mixed, the initial consistency of the mortars was determined by means of the flow-table test (specifically, the truncated cone was raised allowing the concrete to flow out, without applying strokes). Then, nine samples were molded for the tests in the hardened state, whose details are described as follows.

3.3. Macroscale analysis

3.3.1. Macroscopic elastic modulus and strength – static test

For the evaluation of both the overall elastic modulus and the compressive strength six prismatic specimens $40 \times 40 \times 160$ mm^3 were molded. The molding was performed in two layers of 2.0 cm, each one compacted under a cycle of 15 s under vibration on a vibration table. Subsequently, the samples were sealed

Table 3
Chemical composition of ground fly ash (wt.%).

	%
SiO_2	51.9
Al_2O_3	32.8
Fe_2O_3	6.3
CaO	2.7
TiO_2	1.89
K_2O	2.12

Table 4
Material density and mortar mixture composition (in mass and volume).

Material	Density (kg/m^3)	Mass (kg/m^3)		Vol. (dm^3/m^3)	
		C1	C2	C1	C2
Cement	3000	596.2	596.2	198.7	198.7
Quartz filler	2650	223.6	–	84.4	–
Fly ash	1820	–	153.1	–	84.4
ST01/06	2650	633.4	633.4	239.0	239.0
ST06/12	2650	633.4	633.4	239.0	239.0
Admixture	1020	3.4	3.4	3.3	3.3
Water	1000	238.8	238.8	238.8	238.8

Table 5
Mixing procedure.

Procedure	Time (s)
Dry materials mixed together	30
Addition of water	30
Mixture of materials and water	60
Edge shovel clean	30
Addition of superplasticizer	30
Mixture of the base mortar	90

with plastic foil and kept in the mold for 24 h. Later, the specimens were demolded and stored in water for 20 days until the tests in the hardened state were performed. One day before testing, the top and bottom ends of the specimens were polished to obtain flat parallel surfaces.

The uniaxial compression tests were performed by using an electromechanical universal test machine (Testatron, Otto Wolpert-Werke Gmbh). The load was measured by a beam load cell (MTS 100 kN) attached to the electromechanical actuator. Two axial extensometers with gauge length of 25 mm and 50 mm were used to measure the displacement of the specimen. The extensometers were located on the lateral surfaces of the samples as indicated in Fig. 2a. The centric loading was checked at the beginning of the test and, in case of any bending occurrence, the test was stopped and the specimen was adjusted to its center position. The experimental set up is displayed in Fig. 2b. Four loading cycles were performed on each sample to exclude the initial inelasticity (Fig. 3a). The elastic modulus was computed from the linear part of the last cycle in the stress–strain curve, see Fig. 3b. After the third cycle, the loading continued until the ultimate load was reached and the uniaxial compressive strength was then computed.

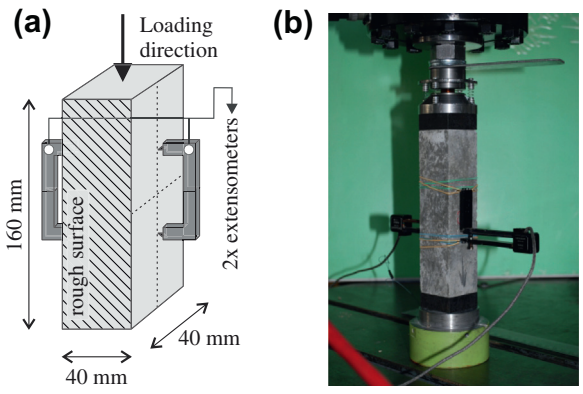

Fig. 2. Elastic modulus tests: (a) specimen dimensions and (b) experimental setup.

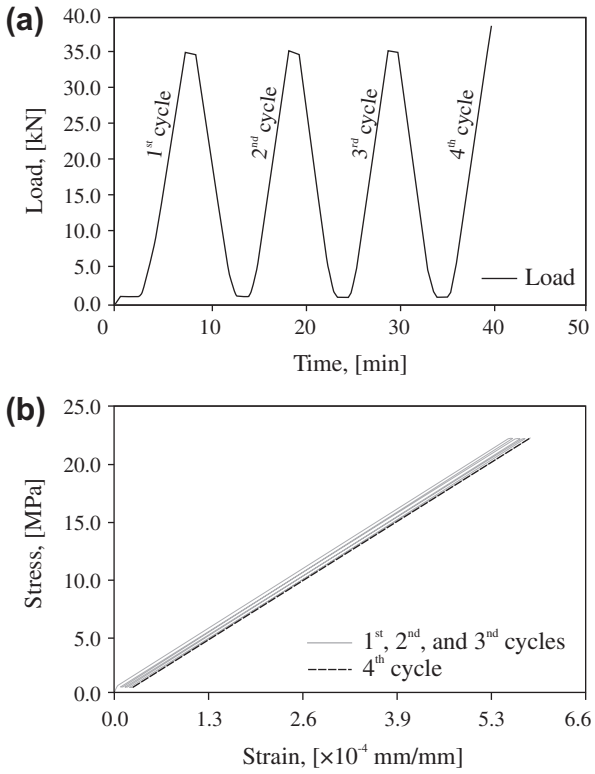

Fig. 3. Elastic modulus: (a) elastic loading cycles and (b) example of compressive stress–strain curve in elastic regime.

3.3.2. Elastic modulus – dynamic test

The dynamic testing described hereafter was used in order to obtain independent results of the macroscopic elastic modulus and the Poisson's ratio and to verify the standard static values. The applied test was proved to be a fast and non-destructive source of information on the macrolevel.

The impulse excitation method used for the assessment of the macroscopic elastic modulus was based on measuring of the fundamental resonant frequencies for longitudinal, transversal, or torsional vibrations of the specimen. The prismatic specimen was always excited by an impact hammer (with recording of the force) on one end, while the acceleration was recorded on the opposite end of the specimen. The signals were analyzed in a frequency domain, and the frequency response function was evaluated after the fast-Fourier transformation. Then, the fundamental resonant frequency was determined. The vibration modes were excited with supports located in the respective nodal positions, i.e. at the midspan for the longitudinal and torsional modes (Fig. 4).

The elastic modulus was evaluated from the equation for longitudinal vibration of the beam with continuously distributed mass with free-free boundary condition as

$$E = \frac{4lmf_l^2}{bt}, \tag{1}$$

where l is the length of the specimen, m is the mass of the specimen, f_l is the fundamental longitudinal resonant frequency of the specimen, b is the width of the specimen, and t is the height of the specimen.

The dynamic shear modulus (G) can be determined by

$$G = \frac{4lmf_l^2}{bt}\left[\frac{B}{1+A}\right], \text{with } B = \left[\frac{b/t + b/t}{4(t/b) - 2.52(t/b)^2 + 0.21(t/b)^6}\right], \tag{2}$$

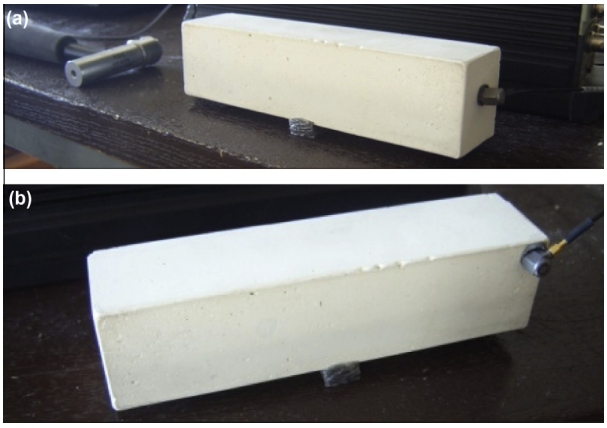

Fig. 4. Setup for the impulse excitation method: (a) longitudinal vibration and (b) torsional vibration.

where f_t is the fundamental torsional resonant frequency of the specimen, A is an empirical correction factor dependent on the width-to-height ratio of the specimen defined in [21].

The Poisson's ratio can then be calculated by

$$v = \frac{E}{2G} - 1. \tag{3}$$

3.4. Microscale analysis

3.4.1. Nanoindentation tests

A cylindrical sample of 30 mm in diameter was prepared for nanoindentation testing (Fig. 5). The molding and curing procedure was held the same as described in Section 3.3.1. The specimen was cut out from the middle section of a larger volume by using a precision diamond saw that provides roughness smaller than 1 μm. Then, the dried surfaces were grinded by SiC papers (grit #2000 and #4000) and polished by cloth with 0.25 μm diamond spray. Finally, the surfaces were cleaned by washing in alcohol and ultrasonic bathing. The resulting surface roughness (root-mean-square) was checked with AFM to be less than 60 nm on 20 × 20 μm area and less than 20 nm on 5 × 5 μm area.

The nanoindentation measurements were carried out in the CSM Nanohardness tester® machine. The three-sided pyramidal indenter tip (Berkovich) was used to perform a massive grids of 16 × 18 = 288 indents with the mutual distance of indents of 8 μm in each (Fig. 6a).

Even if the indentation locations were carefully selected by a high magnification optical microscope prior to testing to ensure that they lie away from large aggregates, part of the grids lay at the place of increased roughness (caused mainly by mechanical effects during polishing) in some cases. If this was the case, such indents were not considered in the final evaluation. The total number of relevant indents reached ≈550, which provided sufficiently large statistical amount of data. The statistical representativeness of the

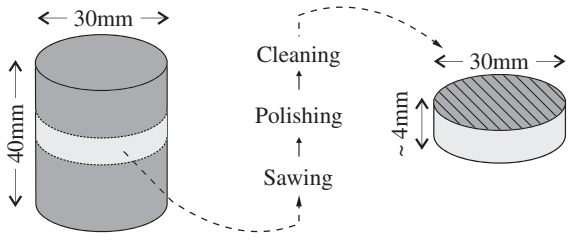

Fig. 5. Specimens for nanoindentation test.

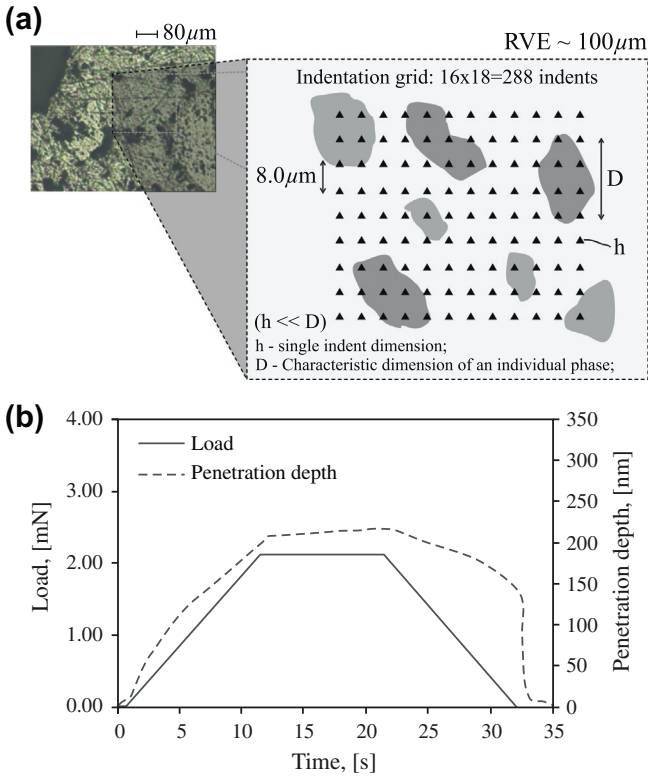

Fig. 6. Nanoindentation tests: (a) indentation grid and (b) loading and penetration depth diagram.

data was also checked successively on datasets consisting of different number of points. It was found that the distribution of elastic stiffness does not fluctuate significantly for datasets containing more than ≈280 indents. Thus, it could be considered as a representative volume element (RVE) on the matrix level (Level I) having the dimension ≈100 μm.

The individual indent size (depth of penetration h) was chosen to be $h \approx 200$ nm [22] so that the affected volume under the indenter, which can be estimated as $3 \times h \approx 600nm$, was smaller than the characteristic sizes of inclusions to avoid significant phase interactions. However, in the dense matrix of a high performance composite, in which several phases of different stiffness occur, full exclusion of interactions can hardly be achieved. Due to surface roughness, which cannot be further decreased by mechanical way [23], the indent size must be kept in hundreds of nm. The indent size of 100–300 nm also suits well the concept of grid indentation on cement pastes [22]. It can be assumed that hard quartz filler or fly-ash particles (of maximum ≈60 μm size) in larger volumes can also cause stiffening of less stiff phases like C–S–H gels during indentation. The error incorporated into the measurements can be roughly quantified by FEM computation as 13–25% [24], which was experimentally justified on an artificial composition of gypsum–zinc composites [24]. Similar errors are incorporated into measurement of stiff inclusions surrounded by a compliant matrix; however, their content is smaller and thus their influence also decreases. It can be assumed that such errors are naturally included in nanoindentation measurements and should be considered in the final comparisons as further discussed in Section 4.

The nanoindentation loading regime contained loading at 12 mN/min, holding for 10 s, and unloading at 12 mN/min (Fig. 6b). The holding period of 10 s with constant force was added mainly to minimize creep effects on the elastic unloading [25]. The elastic modulus of the analyzed phase was determined according to the Oliver–Pharr methodology [10]. The analysis is based on an analytical solution for a cone punched into the elastic isotropic half-space and uses the following equation to define the indentation (reduced) modulus:

$$E_r = \frac{1}{2\beta}\frac{\sqrt{\pi}}{\sqrt{A_c}}S, \tag{4}$$

$$S = \left.\frac{dP}{dh}\right|_{h=h_{max}}, \tag{5}$$

where S, which is defined by Eq. (5), is the contact stiffness assessed as a slope of the unloading branch at the maximum depth h_{max} and the peak load, A_c is the projected contact area at the peak load, and β is the geometrical correction factor introduced to correct the non-symmetrical indenter shape ($\beta = 1.034$ for Berkovich tip). The effect of non-rigid indenter can be taken into consideration by the following equality of compliances

$$\frac{1}{E_r} = \frac{1-\nu^2}{E} + \frac{1-\nu_i^2}{E_i}, \tag{6}$$

where E corresponds to the elastic modulus and ν the Poisson's ratio of the tested materials, while E_i and ν_i are the parameters of the indenter (E_i=1141 GPa and ν_i=0.07 for diamond).

Another material quantity, the hardness H, representing the mean contact pressure under the indenter can be readily obtained from load–deflection indentation curves as

$$H = \frac{P}{A_c}. \tag{7}$$

3.4.2. Deconvolution procedure

The individual phase properties of the analyzed mixtures were determined by applying the statistical deconvolution to elastic modulus histograms [4,22,26]. The results on the elastic moduli in the form of frequency plots are analyzed so that the minimization procedure seeks parameters of n Gauss distributions in an experimental probability density function (PDF), see Fig. 9. In the deconvolution algorithm, a random seed and minimizing criteria based on quadratic deviations between the experimental and theoretically computed overall PDFs are calculated to find the best fit. Details on the deconvolution procedure can be found in [4,26]. The number of the searched phases was fixed to four based on the number of characteristic peaks in the PDF. The dominant phases in the PDF need not necessarily to correlate with the chemically distinct phases and are further considered as mechanically distinct phases used in the homogenization procedure.

3.5. Analytical elastic homogenization

The homogenization corresponds to a technique used to upscale the mechanical properties from the microscale to the upper level to find the effective properties of the RVE. In this paper, the elastic homogenization was performed by means of the analytical Mori–Tanaka scheme [19]. This scheme describes a composite by a morphologically prevailing matrix (the reference medium) reinforced by distinct non-continuous spherical inclusions. Due to its simplicity and the wide range of applicability, the Mori–Tanaka scheme has been successfully used for cementitious materials [17,22]. In the Mori–Tanaka method, the homogenized bulk and shear moduli of a r-phase composite are assessed by the equations that follows

$$k_{\text{hom}} = \frac{\sum_r f_r \cdot k_r (1 + \alpha_0 \cdot (k_r/k_0 - 1))^{-1}}{\sum_r f_r (1 + \alpha_0 \cdot (k_r/k_0 - 1))^{-1}}, \tag{8}$$

$$\mu_{\text{hom}} = \frac{\sum_r f_r \cdot \mu_r (1 + \beta_0 \cdot (\mu_r/\mu_0 - 1))^{-1}}{\sum_r f_r (1 + \beta_0 \cdot (\mu_r/\mu_0 - 1))^{-1}}, \tag{9}$$

$$\alpha_0 = \frac{3 \cdot k_0}{3 \cdot k_0 + 4 \cdot \mu_0}, \tag{10}$$

$$\beta_0 = \frac{6 \cdot k_0 + 12 \cdot \mu_0}{15 \cdot k_0 + 20 \cdot \mu_0}, \tag{11}$$

where the subscript 0 corresponds to the reference medium and r corresponds to a particular inclusion. Thus, k_0 and μ_0 are the bulk and shear moduli of the reference medium, while k_r and μ_r refer to the inclusion phases. The variable f_r corresponds to the volume fraction of the rth phase. These values are the input to the equations that define the homogenized elastic modulus.

Further, the bulk and shear moduli can be recomputed to the elastic modulus and the Poisson's ratio through

$$E_{\text{hom}} = \frac{9 \cdot k_{\text{hom}} \cdot \mu_{\text{hom}}}{3 \cdot k_{\text{hom}} + \mu_{\text{hom}}}, \tag{12}$$

$$\nu_{\text{hom}} = \frac{3 \cdot k_{\text{hom}} - 2 \cdot \mu_{\text{hom}}}{6 \cdot k_{\text{hom}} + 2 \cdot \mu_{\text{hom}}}. \tag{13}$$

3.6. Numerical FFT based elastic homogenization

The numerical scheme used here solves the problem of finding the effective elasticity tensor with a periodically repeating RVE by using discretization of an integral Lippmann–Schwinger equation in the Fourier space. The method, proposed by Moulinec and Suquet [16], leads to the solution of a non-symmetric linear equation system, which can be effectively treated by e.g. the conjugate gradient method [14]. The resulting homogenized elasticity tensor can be compared with the result from the analytical Mori–Tanaka method by assuming macroscopically isotropic material and the plane strain conditions. Then, the analytically computed stiffness matrix (in the Mandel's notation) is given by

$$L^A_{eff} = \frac{E_{\text{hom}}}{(1+\nu_{\text{hom}})(1-2\nu_{\text{hom}})} \begin{bmatrix} 1-\nu_{\text{hom}} & \nu & 0 \\ \nu & 1-\nu_{\text{hom}} & 0 \\ 0 & 0 & 1-2\nu_{\text{hom}} \end{bmatrix}, \tag{14}$$

where E_{hom} and ν_{hom} are the homogenized (Mori–Tanaka) elastic modulus and Poisson's ratio, respectively (Eqs. (12) and (13)). The difference between this analytical solution and the numerically obtained solution (denoted as L^{FFT}_{eff}) can be evaluated through the following metrics

$$\delta = \sqrt{\frac{\left(L^{FFT}_{eff} - L^A_{eff}\right) :: \left(L^{FFT}_{eff} - L^A_{eff}\right)}{\left(L^{FFT}_{eff} :: L^{FFT}_{eff}\right)}} \tag{15}$$

4. Results

4.1. Experimental results – Macroscale analysis

The flow table tests for the C1 and C2 are of 175 and 245 mm, respectively, indicating that the use of fly ash in C2 resulted in increased workability. This tendency is in agreement with the results published in [27,28].

The results of elastic modulus obtained from the uniaxial compression tests are summarized in Table 6. Considering these results, and based on the Student's t-test [29] with a significance level set at 5.0%, it can be concluded that the elastic modulus of C1 is greater than that of C2.

The results of the dynamic elastic modulus obtained by the impulse excitation method with longitudinal vibration (Eq. (1)) are also presented in Table 6. Due to the physical nature of the test (i.e. higher loading rate), the dynamic elastic modulus is usually greater than the elastic modulus obtained from the static test. However, excellent agreement of the two methods, within 6.0%, for our samples was attained. The impulse method also provides an estimate of the sample Poisson's ratio (Eq. (3)), which was found to be 0.18 and 0.19 for C1 and C2, respectively.

Table 6 also shows the strength results measured in the uniaxial compression tests. The results indicate that, at the age of 21 days, the mixture produced with quartz filler (C1) attained greater compressive strength than the one produced with fly ash (C2). These results correlate with the results of elastic moduli (static and dynamic) of the fly ash reinforced mixture (C2), which is mainly due to the higher total porosity.

4.2. Experimental results – Microscale analysis

4.2.1. Nanoindentation

Regarding the microscale measurements, 550 indents to the cementitious matrix were performed in total. Examples of the load–penetration curves and related load/penetration–time diagrams showing indents to differently stiff phases are presented in Figs. 7 and 8. All relevant indents were analyzed by the Oliver–Pharr method [10] for an elastic modulus with the assumption of constant Poisson's ratio 0.20 for all indents since the influence of the selected Poisson's ratio in the relevant range 0.18–0.22 on the evaluation is very small [17]. Subsequently, the frequency plots of elastic moduli (bin size =1.0 GPa) and related experimental probability density functions (PDFs) were computed for both samples. The deconvolution method was applied to PDFs as illustrated in Fig. 9. The numerical results containing the elastic moduli and volume fractions are listed in Table 7.

As mentioned above, the results are considered as results received on mechanically distinct phases and there is no intention to link them with pure chemical phases, such as C–S–H gels with different densities, Portlandite, interfacial zones, and interfacial zones [5,17,22]. Aside the clinker and fly ash residues in C2, the majority of the hydrated volume in our samples is composed of C–S–H gels and partly $Ca(OH)_2$. The volume of $Ca(OH)_2$ is decreased compared to pure Portland cement hydration since a large amount of Portlandite in C2 samples is consumed in the pozzolanic reaction with fly ash [30]. However, it is still present in some extent dispersed in the C–S–H phase. Although the results from the deconvolution present mechanically distinct phases rather than the chemically distinct phases, they are closely related.

Based on the SEM imaging, cement chemistry, and mixture composition, it is assumed that the **phase A** in Fig. 9 is composed of low stiffness porous phases, the **phase B** contains the majority of the main hydration products (C–S–H gels and partly $Ca(OH)^2$), the **phase C** is composed of high stiffness hydration products (high stiffness C–S–H and partly $Ca(OH)_2$), and the **phase D** contains the remaining non-hydrated clinker, fly ash (C2) or quartz filler (C1).

Table 6
Macroscale measurements – Elastic modulus (E_s – static, E_d – dynamic) and compressive strength (f_c).

Sample	E_s (GPa)		E_d (GPa)		f_c (MPa)	
	C1	C2	C1	C2	C1	C2
1	41.2	35.9	42.4	36.5	61.4	53.5
2	38.1	33.3	40.6	35.5	58.2	44.3
3	37.5	33.1	41.6	38.0	49.4	46.2
4	39.1	36.5	–	–	57.0	42.7
5	38.8	34.2	–	–	55.7	46.2
6	39.5	36.4	–	–	54.7	51.6
$\bar{X}$[a]	39.0	34.9	41.5	36.7	56.1	47.4
s_d[a]	1.28	1.54	0.91	1.27	4.0	4.2

[a] $\bar{X}$ – average value, s_d– standard deviation.

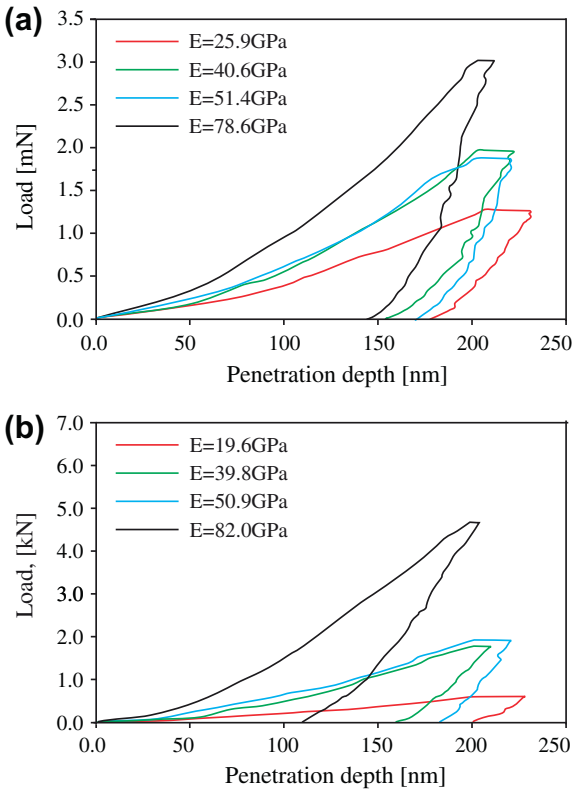

Fig. 7. Example of load–penetration curves obtained for (a) C1 and (b) C2.

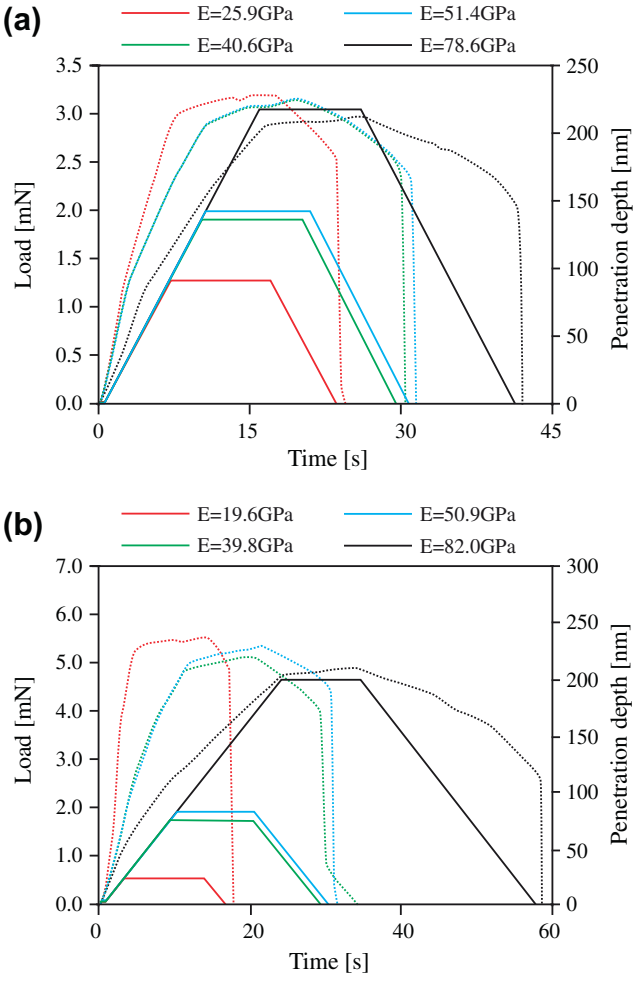

Fig. 8. Load and depth of penetration versus time: (a) C1 and (b) C2.

The original ill-posed problem of the deconvolution into infinite number of distributions is regularized by using the aforementioned four phases having a clear physical meaning related to the microstructural composition. The mechanically distinct phases are represented by significant peaks in the experimental PDF of elastic moduli and are identified by the minimization procedure in the deconvolution algorithm. The deconvolution procedure was further checked by using the same methodology to hardness measurements (0.1GPa bin size was assumed in the construction of PDF). The algorithm converged to the qualitatively analogous distributions of the four phases (Fig. 9) and and thus the results were found to be consistent with the results obtained for elastic modulus. The numerical results of the mean hardness values estimated for individual mechanical phases are summarized in Table 7.

Due to unavoidable phase interactions, the elastic moduli do not represent the exact material constants for pure phases, which is manifested mainly for the stiffest components, such as the clinker, whose elastic modulus reaches ≈130 GPa on a pure clinker sample [25,31]. However, the separation of the mechanical performance of the individual components is not possible from the measured response, and the influence of interactions can be just estimated as mentioned in Section 3.4.1. Further, the evaluated micromechanical values are considered as the first estimates and as such they neglect the interaction phenomena in the following upscaling.

4.2.2. Homogenization

The microstructure of the analyzed composites was separated in two levels. Firstly, the matrix level (denoted as Level I) is characterized by all the matrix phases having characteristic dimensions less than $d \approx 10$ μm (i.e. hydration products, clinker, quartz filler, and fly ash). The RVE size (L), which also corresponds to the indentation grid, has the dimension ≈100 μm. Therefore, the scale separability condition $h \ll d \ll L$ [12,22], where h is the indent size, d is the characteristic inclusion size, and L is the RVE size, holds. The situation is shown in Fig. 10.

Since the volume affected by the indentation is of ≈0.6 μm^3, it is assumed that all the pores smaller than this limit are naturally included in the indentation results. It includes mainly nanoporosity. However, a small part of pores with the dimension of 0.6–10 μm (i.e. 1/10 RVE) also lies in the Level I but cannot be detected by the nanoindenter. Therefore, this porosity was included as an additional mechanical phase in the Level I (Table 8).

Mercury intrusion porosimetry (MIP) performed on the crushed pieces of the composites of the size of up to 5 mm was used for assessment of the Level I porosity (i.e. pores in the range from 0.6 μm to 10 μm), which equaled to 2.4 vol.% for C1 and 3.3 vol.% for C2 (Fig. 11). The results obtained for the homogenized elastic modulus and the Poisson's ratio by using the Mori–Tanaka method for the Level I are presented in Table 8. The isotropic stiffness matrix (computed using Eq. (14)) is then

$$L^A_{eff} = \begin{bmatrix} 51.0 & 12.8 & 0 \\ 12.8 & 51.0 & 0 \\ 0 & 0 & 38.3 \end{bmatrix},$$

for C1, and the corresponding effective stiffness matrix calculated by the FFT method resulted in

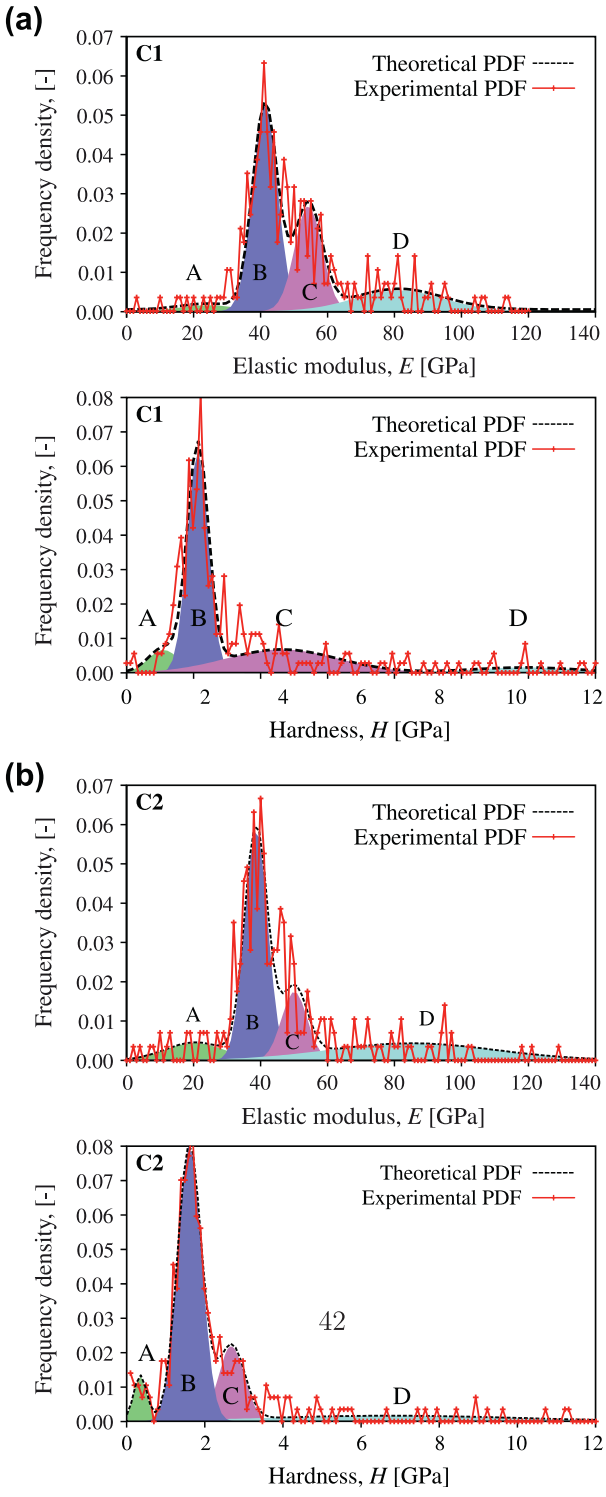

Fig. 9. Experimental and best-estimated PDF obtained by deconvolution of elastic modulus (bin size 1.0 GPa) and hardness (bin size 0.1 GPa): (a) C1 and (b) C2.

$$L_{eff}^{FFT} = \begin{bmatrix} 52.4 & 13.3 & 0.2 \\ 13.3 & 52.3 & 0.1 \\ 0.2 & 0.1 & 39.3 \end{bmatrix}.$$

In the case of C2, the isotropic stiffness matrix was

$$L_{eff}^{A} = \begin{bmatrix} 45.2 & 11.3 & 0 \\ 11.3 & 45.2 & 0 \\ 0 & 0 & 33.9 \end{bmatrix},$$

Table 7
Elastic modulus (E), volume fraction (V_{frac}), and Hardness (H) obtained by deconvolution.

Mixture	Phases	E (GPa)	s_{d_E} (GPa)	H (GPa)	s_{d_H} (GPa)	V_{frac} (%)
C1	A	24.4	8.35	0.95	0.39	6.3
	B	41.3	3.70	1.83	0.27	48.8
	C	54.3	4.07	3.98	1.44	27.4
	D	81.2	13.29	10.19	1.39	17.5
C2	A	20.3	8.86	0.25	0.17	9.8
	B	38.7	3.43	1.52	0.31	50.5
	C	50.1	3.84	2.61	0.34	22.8
	D	85.2	25.17	6.73	3.29	16.8

and the corresponding effective stiffness matrix (FFT method) resulted in

$$L_{eff}^{FFT} = \begin{bmatrix} 44.3 & 13.0 & 0.6 \\ 13.0 & 44.4 & -0.1 \\ 0.6 & -0.1 & 32.7 \end{bmatrix}.$$

The application of the FFT-based numerical scheme resulted in the effective stiffness matrix (Level I) which was very consistent with the analytical results. The difference of the methods given by the metrics (Eq. (15)) was 1.5% for C1 and 4.3% for C2, respectively. Due to very low anisotropy of the matrices, the FFT-based results can be directly compared with the analytical prediction (Eq. (14)) and and effective isotropic moduli estimated in the range of 47.1–47.2 GPa for C1 and 39.2–39.9 GPa for C2.

Next, the level of the whole mortar (denoted as Level II) was constructed. It consisted of the homogenized phase of the Level I (matrix) and the rest of components, i.e. large sand particles, aggregates, and air voids (capillary pores with diameter greater than 10 μm and large air voids coming from entrapped air greater than 1 mm). Since the aggregate does not change chemically in the composite, its portion is given by the initial mixture proportions (Table 4). The elastic modulus and the Poisson's ratio of the quartz aggregates were assumed as 71.8 GPa and 0.17 respectively [32]. Sometimes, an additional phase, i.e. an interfacial zone between the matrix and the aggregate, is considered as a separate phase in multiscale models. In our case, the properties of possible ITZ are naturally included in the nanoindentation data because the indentation grid was squeezed between the large aggregate. Also, the very dense matrix itself consists of possibly interconnecting ITZs surrounding the pure phases.

Due to the large span of the pore diameters ranging from μm to mm, a combination of imaging techniques was used to assess the Level II porosity. Image analysis was employed to segmented back-scattered (BSE) electron and optical images (OI). The segmentation was performed on the thresholded binary images, where the pores are represented by black pixels. The medium size porosity (10 μm to 1.0 mm) was assessed from 25× magnification BSE images. The threshold value used in the BSE images was set at 100 to 110 and the pores that were observed in the aggregates were not considered in the total porosity of the matrix. Fifteen different BSE images were analyzed and the results averaged. The analysis yielded 8.92% of porosity for C1 and 11.25% of porosity for C2 (Table 9).

The pores larger than 1 mm (mainly entrapped air pores) were assessed similarly from optical images (OI) with 10× magnification. In particular, prior to grayscale conversion, the image contrast was enhanced by using a bottom-hat filtering and a contrast adjustment function, which provides optimized results when image segmentation is applied. A similar method has been applied in [33] to compute the percentage of voids on concrete surface. A comprehensive review about image analysis techniques for civil engineering materials is available in [34]. Next, the threshold value was set at 200–210 and the percentage of pores was computed.

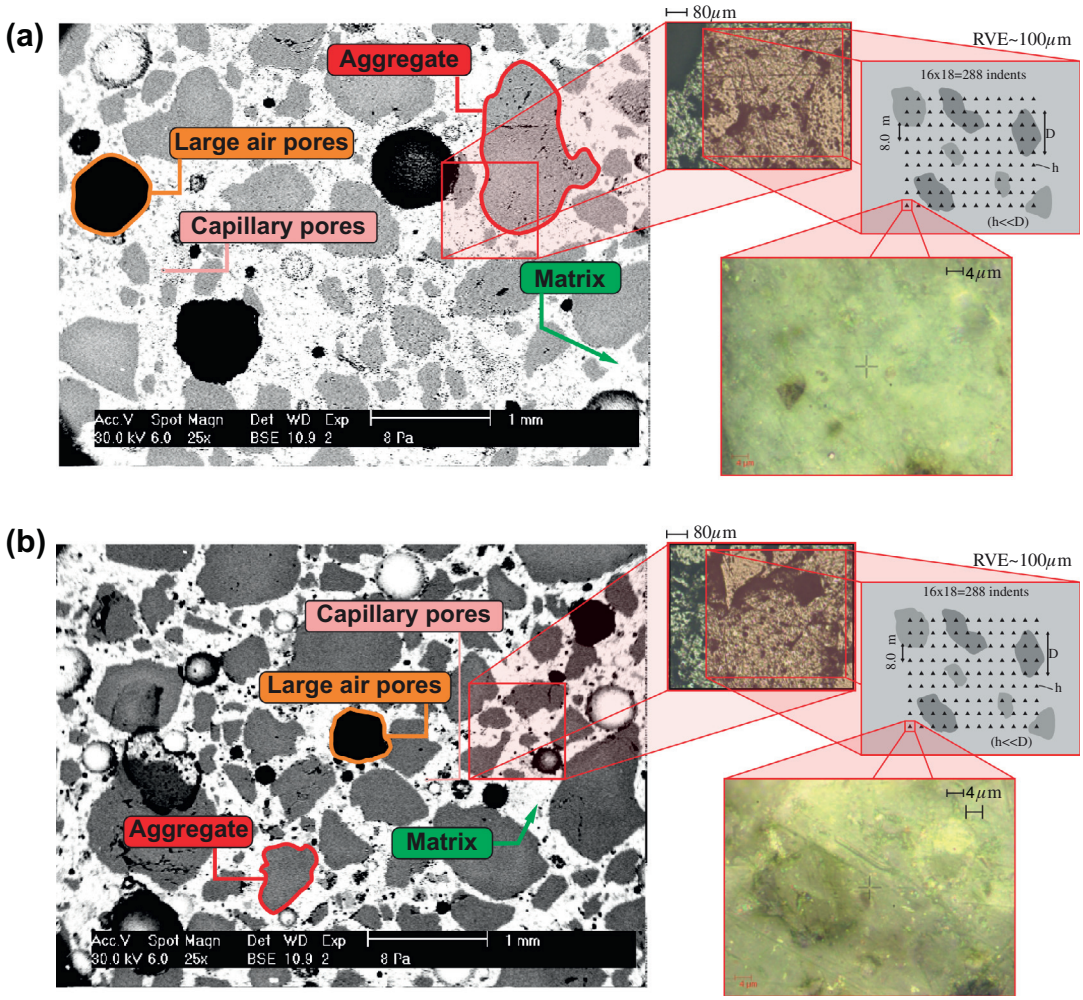

Fig. 10. Scale definition for (a) C1 and (b) C2.

Table 8
Mechanical properties of the Level I obtained by homogenization.

	Phase	E (GPa)	v (–)	V_{frac} (%)	V'_{frac} [a] (%)	Mori–Tanaka		FFT
						E_{hom}^{Level} (GPa)	v_{hom}^{Level} (-)	E_{hom}^{Level} (GPa)
Level I - C1	A	24.4	0.20	6.3	6.2	45.9	0.20	47.1–47.2
	B	41.3	0.20	48.8	47.6			
	C	54.3	0.20	27.4	26.7			
	D	81.2	0.20	17.5	17.1			
	Porosity	-	-	-	2.4			
Level I - C2	A	20.3	0.20	9.8	9.5	40.7	0.20	39.2–39.9
	B	38.7	0.20	50.5	48.9			
	C	50.1	0.20	22.8	22.1			
	D	85.2	0.20	16.8	16.3			
	Porosity	-	-	-	3.3			

[a] V'_{frac}-corrected volume fraction with respect to added porosity.

The analysis resulted in 0.31% of porosity for C1 and 0.47% of porosity for C2 (Table 9).

The results obtained for the homogenized elastic modulus and the Poisson's ratio by using the Mori–Tanaka method are presented in Table 9 for the Level II.

5. Verification and validation of the proposed methodology

The verification and validation of the proposed methodology is based on the comparison of the elastic modulus obtained from the Level II homogenization (Table 9) and and the one obtained from macroscopic tests (Table 6). These results, which are summarized in Table 10, indicate similar trend, i.e. the elastic modulus (as well as the compressive strength) of C2 is lower than that of C1, which can be observed for all the methods. Because the proposed methodology allowed for determining the macroscopic elastic properties of C1 and C2, and also the difference between them, this can be considered reliable. The relative error between the results obtained from the macroscale elastic modulus tests and homogenized values is within the order of tens of percent for both static

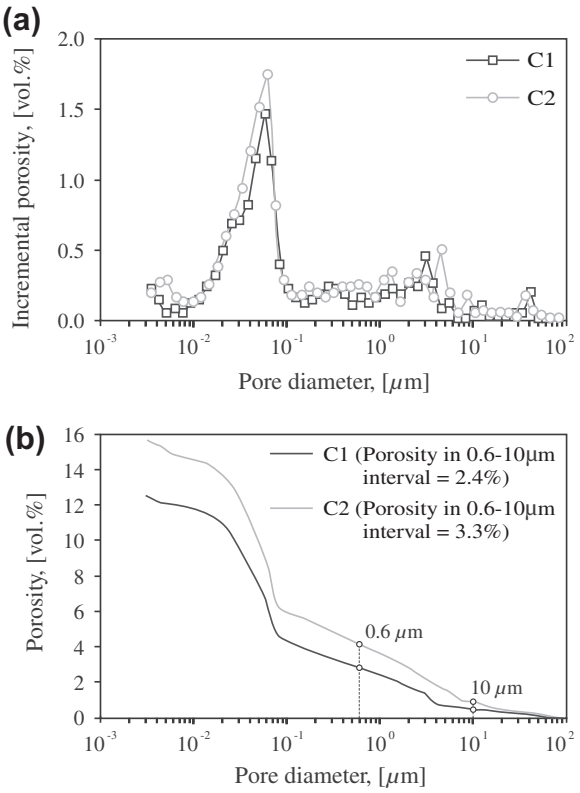

Fig. 11. Mercury intrusion porosimetry: (a) incremental porosity curve and (b) cumulative porosity curve.

and dynamic analyses (see Table 10). Despite the average difference ($\bar{\delta}_{error}$) of 14.9% and 14.3% between upscaled (E_{hom}) and measured (E_s and E_d) values for C1 and C2, respectively, the results are correct and realistic.

As mentioned in Section 3.4.1, the evaluation of nanoindentation tests is not error-free. In the case of HPCC, which consists of a dense matrix with several phases of different stiffness and also interfacial (matrix/aggregate) zones, the interaction between the matrix and these phases can affect the final nanoindentation results. Therefore, it can be assumed that the error presented in Table 10 is caused by the phase interactions influencing the nanoindentation results. The influence of the evaluation by deconvolution is also considered. This observation is supported by the following facts. The macroscopic results were verified by two independent techniques: the static compression test and the dynamic impulse method, and both have shown similar results. The homogenization of the Level I was also verified with the numerical FFT-based method, which provided similar results to those obtained with the analytical Mori–Tanaka scheme (1.5–4.3% difference). The Level II homogenization was based on mixture proportions and independent image analysis results. Thus, the overall error

Table 10
Elastic modulus: Homogenization vs. Macroscale tests.

	E_{hom} (GPa)	E_s (GPa)	E_d (GPa)	δ_{E_{hom}/E_s} (%)	δ_{E_{hom}/E_d} (%)	$\bar{\delta}_{error}$ (%)
C1	46.2	39.0	41.5	18.5	11.3	14.9
C2	40.9	34.9	36.7	17.2	11.4	14.3

must come from the basic indentation data used in the Level I homogenization. To decrease the phase interactions effect and thus refine the computations in their quality, it would be necessary to decrease the size of indents (provided that the surface had smaller roughness). Nevertheless, such refinement is hardly achievable with standard polishing techniques that provide surface roughness at least in the order of several tens of nanometers on the given sample composition.

Despite the presence of error, the use of nanoindentation tests cannot not be either discarded or substituted since it corresponds to the best experimental technique that allows for direct assessing of the mechanical properties of material volumes with dimensions on the nanometer scale [3], reason why this technique has been chosen in the presented research.

6. Conclusions

In this paper, a prediction methodology has been described and applied for determining the macroscale elastic properties of HPCC based on multiscale analysis. Depending on the obtained results the following conclusions can be drawn.

The experimental results showed that the use of statistical grid nanoindentation, which was used for the mechanical analysis on the microscale level, can be performed in a very effective way on the matrix components and can provide reliable estimates of their stiffness.

Moreover, it has been proved that the combination of several independent experimental techniques listed in the proposed methodology (i.e. the basic micromechanical data as well as porosimetry and image analysis and their combination in the homogenization procedures) offers a cost effective tool for virtual testing of macroscale mechanical performance of HPCC, which includes a mix of different chemical and mechanical phases. This feature can be attractive to the concrete industry since the use of the proposed methodology would dramatically reduced the total volume of initial experimental work spent to perform the analysis of the composite and, more important, it would enable the production of a more predictable composite, in this case, a more predictable high performance concrete in regard to macroscale elastic properties.

Acknowledgements

The support of the project OP VK CZ.1.07/2.3.00/30.0034 "Support for improving teams in research and development and the

Table 9
Mechanical properties of the Level II obtained by homogenization.

	Phase	E (GPa)	ν (-)	V_{frac} (%)	$E_{hom}^{LevelII}$ (GPa)	$\nu_{hom}^{LevelII}$ (-)
Level II - C1	Level I – homogenized matrix	45.9	0.20	47.6	46.2	0.18
	Aggregate (0.10–1.25 mm)	71.8	0.17	43.2		
	Capillary pores > 10 μm – 1*mm* (BSE)	-	-	8.92		
	Large air pores > 1 mm (OI)	-	-	0.31		
Level II - C2	Level I – homogenized matrix	40.7	0.20	46.3	40.9	0.18
	Aggregates (0.10–1.25 mm)	71.8	0.17	42.0		
	Capillary pores > 10 μm – 1*mm* (BSE)	-	-	11.25		
	Large air pores > 1 mm (OI)	-	-	0.47		

development of intersectoral mobility at Czech Technical University in Prague" and Czech Science Foundation (Project P105/12/0824) is gratefully acknowledged. Also, the authors wish to acknowledge the staff members at the CTU in Prague, especially Ing. Pavel Reiterman, RNDr. Lubomír Kopecký and Dr. Tomáš Plachý for their help with experimental measurements.

References

[1] Taylor H. Cement chemistry. 2nd ed. Academic Press; 1990.
[2] Jennings HM. A model for the microstructure of calcium silicate hydrate in cement paste. Cem Concr Res 2000;30(1):101–16. http://dx.doi.org/10.1016/676S0008-8846(99)00209-4.
[3] Němeček J. Nanoindentation of heterogeneous structural materials – habilitation thesis. ČVUT Prague: CTU Reports; 2010.
[4] Němeček J, Šmilauer V, Kopecký L. Nanoindentation characteristics of alkali-activated aluminosilicate materials. Cem Concr Compos 2011;33(2):163–70. http://dx.doi.org/10.1016/j.cemconcomp.2010.10.005.
[5] Constantinides G, Ulm FJ. The effect of two types of C–S–H on the elasticity of cement-based materials: Results from nanoindentation and micromechanical modeling. Cem Concr Res 2004;34(1):67–80. http://dx.doi.org/10.1016/S0008-8846(03)00230-8.
[6] Calabri L, Pugno N, Valeri S. AFM nanoindentation method: geometrical effects of the indenter tip. In: Applied scanning probe methods XI. Nanoscience and technology. Berlin Heidelberg: Springer; 2009. p. 139–64.
[7] Scrivener KL. Backscattered electron imaging of cementitious microstructures: understanding and quantification. Cem Concr Compos 2004;26(8):935–45. http://dx.doi.org/10.1016/j.cemconcomp.2004.02.029.
[8] Chen JJ, Sorelli L, Vandamme M, Ulm FJ, Chanvillard G. A coupled nanoindentation/SEM-EDS study on low water/cement ratio portland cement paste: evidence for C–S–H/Ca(OH)2 nanocomposites. J Am Ceram Soc 2010;93(5):1484–93. http://dx.doi.org/10.1111/j.1551-2916.2009.03599.x.
[9] Fischer-Cripps AC. Nanoindentation. 3rd ed. Springer; 2002.
[10] Oliver WC, Pharr GM. An improved technique for determining hardness and elastic modulus using load and displacement sensing indentation experiments. J Mater Res 1992;7(6):1564–83. http://dx.doi.org/10.1557/JMR.1992.1564.
[11] Vandamme M, Ulm FJ. Viscoelastic solutions for conical indentation. Int J Solids Struct 2006;43(10):3142–65. http://dx.doi.org/10.1016/j.ijsolstr.2005.05.043.
[12] Zaoui A. Continuum micromechanics: survey. J Eng Mech 2002;128(8):808–16. doi:http://dx.doi.org/10.1061/(ASCE)0733-9399(2002)128:8(808).
[13] Eshelby JD. The determination of the elastic field of an ellipsoidal inclusion, and related problems. Proc R Soc London Ser A Math Phys Sci 1957;241:376–96. http://dx.doi.org/10.1098/rspa.1957.0133.
[14] Zeman J, Vondřejc J, Novák J, Marek I. Accelerating a FFT-based solver for numerical homogenization of periodic media by conjugate gradients. J Comput Phys 2010;229(21):8065–71. http://dx.doi.org/10.1016/j.jcp.2010.07.010.
[15] Garboczi EJ. Finite element and finite difference programs for computing the linear electric and elastic properties of digital images of random materials. Building and Fire Research Laboratory – National Institute of Standards and Technology; 1998.
[16] Moulinec H, Suquet P. A fast numerical method for computing the linear and nonlinear mechanical properties of composites. C R l' Académie Sci, Ser II Univers 1994;318(11):1417–23.
[17] Sorelli L, Constantinides G, Ulm FJ, Toutlemonde F. The nano-mechanical signature of ultra high performance concrete by statistical nanoindentation techniques. Cem Concr Res 2008;38(12):1447–56. http://dx.doi.org/10.1016/j.cemconres.2008.09.002.
[18] Bharatkumar BH, Narayanan R, Raghuprasad BK, Ramachandramurthy DS. Mix proportioning of high performance concrete. Cem Concr Compos 2001;23(1):71–80. http://dx.doi.org/10.1016/S0958-9465(00)00071-8.
[19] Mori T, Tanaka K. Average stress in matrix and average elastic energy of materials with misfitting inclusions. Acta Metall 1973;21(5):571–4. http://dx.doi.org/10.1016/0001-6160(73)90064-3.
[20] da Silva WRL, Damo G, Oliveira AL, Tochetto E, Prudencio LR. Influence of air temperature on the performance of different water reducing admixtures with respect to the properties of fresh and hardened mortar. Adv Civil Eng 2010;2010(2010):1–10. http://dx.doi.org/10.1155/2010/136768.
[21] ASTM E1876-01. Standard test method for dynamic Young's modulus, shear modulus, and Poisson's ratio by impulse excitation of vibration; 2006.
[22] Constantinides G, Chandran KSR, Ulm FJ, Vliet KJV. Grid indentation analysis of composite microstructure and mechanics: principles and validation. Mater Sci Eng A 2006;430(1-2):189–202. http://dx.doi.org/10.1016/j.msea.2006.05.125.
[23] Miller M, Bobko C, Vandamme M, Ulm FJ. Surface roughness criteria for cement paste nanoindentation. Cem Concr Res 2008;38(4):467–76. http://dx.doi.org/10.1016/j.cemconres.2007.11.014.
[24] Němeček J, Lukeš J. On the evaluation of elastic properties from nanoindentation of heterogeneous systems. Chem Listy 2010;104(S):279–82.
[25] Němeček J. Creep effects in nanoindentation of hydrated phases of cement pastes. Mater Charact 2009;60(9):1028–34. http://dx.doi.org/10.1016/j.matchar.2009.04.008.
[26] Němeček J, Králík V, Vondřejc J. Micromechanical analysis of heterogeneous structural materials. Cem Concr Compos 2013;36(0):85–92. http://dx.doi.org/10.5772/5096810.1016/j.cemconcomp.2012.06.015.
[27] Nochaiya T, Wongkeo W, Chaipanich A. Utilization of fly ash with silica fume and properties of portland cement–fly ash–silica fume concrete. Fuel 2010;89(3):768–74. http://dx.doi.org/10.1016/j.fuel.2009.10.003.
[28] Ravina D, Mehta PK. Properties of fresh concrete containing large amounts of fly ash. Cem Concr Res 1986;16(2):227–38. http://dx.doi.org/10.1016/0008-8846(86)90139-0.
[29] Montgomery DC, Runger GC. Applied statistics and probability for engineers. 5th ed. Wiley; 2010.
[30] Sakai E, Miyahara S, Ohsawa S, Lee SH, Daimon M. Hydration of fly ash cement. Cem Concr Res 2005;35(6):1135–40. http://dx.doi.org/10.1016/j.cemconres.2004.09.008.
[31] Velez K, Maximilien S, Damidot D, Fantozzi G, Sorrentino F. Determination by nanoindentation of elastic modulus and hardness of pure constituents of portland cement clinker. Cem Concr Res 2001;31(4):555–61. http://dx.doi.org/10.1016/S0008-8846(00)00505-6.
[32] Fukuhara M, Sanpei A, Shibuki K. Low temperature-elastic moduli, debye temperature and internal dilational and shear frictions of fused quartz. J Mater Sci 1997;32(5):1207–11. http://dx.doi.org/10.1023/A:1018583918380.
[33] da Silva WRL, Štemberk P. Expert system applied for classifying self-compacting concrete surface finish. Adv Eng Software 2013;64(0):47–61. http://dx.doi.org/10.1016/j.advengsoft.2013.04.005.
[34] Coster M, Chermant JL. Image analysis and mathematical morphology for civil engineering materials. Cem Concr Compos 2001;23(2001):133–51. http://dx.doi.org/10.5772/5096810.1016/S0958-9465(00)00058-5.